Controls on the deep water cycle within three-dimensional mantle convection models

Matthew G. Price[1], J. H. Davies[1], James Panton[1]

[1]School of Earth and Ocean Sciences, Cardiff University, Main Building, Park Place, Cardiff, CF10 3AT, Wales, UK.

Key Points:

- Water cycling is implemented into a 3-D mantle convection model
- Water storage capacity of the mantle is shown to be insensitive to many of the investigated model parameters
- The mantle at present day is found to contain approximately twice the water of today's oceans

Corresponding author: J. H. Davies, `daviesjh2@cardiff.ac.uk`

Abstract

Earth's mantle is known to harbour water in the form of hydrous and nominally anhydrous minerals. How much water the mantle holds and whether it has remained constant through time are open questions. Previous numerical studies of the deep-water cycle have been limited to box models or 2-D calculations. Here we present for the first time, results from 3-D mantle convection models. We address the evolution of the mantle's total water content by adapting a well benchmarked mantle convection code to track water, including its feedbacks on dynamics. While Earth's surface is presently covered by one ocean mass of water, our results suggest that the mantle holds approximately two ocean masses of water based on the best estimates from mineral physics. This value varies only weakly for a wide parameter space of additional complex dynamics such as; viscosity laws, density controls and phase change considerations. Our result of a mantle holding two ocean masses conforms with estimates from other branches of earth science, suggesting that these models could be an excellent tool in understanding the spatial heterogeneity of the water found in the mantle.

Plain Language Summary

Water is known to exist within Earth's interior thanks to measurements made on rocks known to have come from the planet's interior. The total amount of water that is found within the planet is however, only roughly estimated. This amount of water is measured as a multiple of the water that we know exists on Earth's surface; this is known as an ocean mass. In our work, we employ computer models that model the mantle in order to provide a better estimate of the number of ocean masses inside the planet. By running many models, our results suggest that the mantle contains roughly two present day ocean masses of water. This result agrees with the amount of water estimated to be in the mantle from other branches of Earth and Planetary Science and is important in helping to understand how common water is in rocky planets.

1 Introduction

The presence of water on a planetary body is a well used constraint on the likelihood of a habitable planet (Maruyama et al., 2013; McKay, 2014; Tackley, Ammann, Brodholt, Dobson, & Valencia, 2012). For Earth, there is clearly a significant amount of water existing at and above the planet's surface, approximately 1.4×10^{21} kg of wa-

ter, or one ocean mass (1 OM). However, we also know there must be water being held deeper within the planet from the surface to the core-mantle boundary (CMB) as can be seen from measurements of rock samples and volcanic gases (Hirschmann, 2006). This partitioning of water between the planet's surface and interior will influence many mantle processes due to its effects on the physical properties of the mantle.

For instance, the presence of water is known to alter the temperature at which mantle material will undergo melting, as melting solidi are lowered in the presence of water (e.g. J. H. Davies & Bickle, 1991; Katz, Spiegelman, & Langmuir, 2003). Furthermore, numerous studies have detailed the role water plays in weakening mantle material (e.g. Korenaga & Karato, 2008; Mei & Kohlstedt, 2000), although its effect on lower mantle rheology is likely to be minimal (Muir & Brodholt, 2018). Whilst water-rich material is likely to be lighter than dry material, the density influence of water on mantle flow is anticipated to be less important compared to the density contrasts between ambient and basaltic material (up to 1% compared to 2–5+%) (Nakagawa, Nakakuki, & Iwamori, 2015).

In order to better understand the deep-water system, many studies have utilised dynamic models as an approach to help understand this system. One-dimensional, parameterisations of mantle convection have been used to great effect in understanding the feedback trends water has on mantle evolution. McGovern and Schubert (1989) is an early study that looked at the effects of volatile exchange between the mantle and surface reservoir on the thermal evolution of the mantle. They determined that the degassing and regassing of volatiles equilibrate early on in Earth evolution. Furthermore, by considering a water-dependent viscosity they found that the evolving thermal state of the mantle is linked to these volatile exchange rates, with net degassing/regassing linked to a hotter/colder mantle. More recent parameterised model studies (e.g. Crowley, Gérault, & O'Connell, 2011; Sandu, Lenardic, & McGovern, 2011), have considered the relationship between the temperature and the resulting concentration of water in the mantle, as well as producing estimates on the global water budget (with studies suggesting values in the region 1–2 OM).

The most sophisticated dimensional modelling of the deep-water system in the mantle have so far been in a 2-D cylindrical geometry (e.g. Nakagawa, Iwamori, Yanagi, & Nakao, 2018; Nakagawa et al., 2015). Dimensional models allow more nuanced insights into the spatial distribution of water within the mantle. By incorporating estimates of

water storage capacities of the different mantle material for different pressures and temperatures (such as the water solubility phase diagrams in Iwamori, 2007) these 2-D models have been able to investigate the effect of water dependent viscosities and densities on the dynamics of the mantle system. Nakagawa and co-authors have also used these 2-D models to investigate the global water budget, and contrary to the 1-D, analytical studies, arrive at an estimate for the total mantle water budget lying between 9–12 OM.

As can be seen, there is a clear disparity in the prediction of the mass of water in the mantle between analytical and dimensional models. Therefore, in this study we endeavour to build on the previous work by employing, for the first time, three-dimensional numerical models to determine an estimate of the mantle water budget. By using 3-D geometry, we will be able to explore the transportation of water through the mantle in a much more realistic setting with along strike downwellings and matching plume features when compared to the lower dimension models.

2 Methodology

2.1 Numerical Modelling

The time-dependent mantle convection flow field is solved using the governing equations for mantle convection (Mckenzie, Roberts, & Weiss, 1974) and the robust three-dimensional mantle convection code TERRA (Baumgardner, 1985; Bunge & Baumgardner, 1995; Bunge, Richards, & Baumgardner, 1997; D. R. Davies et al., 2013). Calculations were performed on a mesh with over 10 million grid points, giving an average grid spacing of 45 km over the whole mantle volume. At this grid resolution we are able to investigate models which are at Earth-like vigour ($Ra \approx 10^8$), with the viscosity, η, given by a combination of depth (d), temperature (T) and water weight % (C_w) viscosity factors such that

$$\eta(d, T, C_w) = \eta_0 \times \eta_d \times \eta_T \times \eta_w \tag{1}$$

Relevant model parameters are listed in Table 1.

The movement of water and bulk composition is tracked using particles. With ≈ 100 million active particles we ensure adequate coverage over the entire numerical domain. Using particles we track a continuous mantle bulk composition range (from entirely depleted up to enriched basaltic content), the accurate movement of water content, as well as heat generating elements (isotopes of U, Th, K).

Table 1. Reference case (incompressible) model parameters.

Parameter	Symbol	Value	Units
Surface temperature	T_S	300	K
Core-mantle boundary (CMB) temperature	T_{CMB}	3000	K
Internal heating rate	H	4×10^{-12}	W kg^{-1}
Reference viscosity	η_0	2×10^{21}	Pa s
Lithosphere viscosity factor	η_{lith}	50	–
Lower mantle viscosity factor	η_{660}	30	–
Density	ρ	4500	Kg m^{-3}
Thermal expansivity	α	2.5×10^{-5}	K^{-1}
Thermal conductivity	k	4	W m^{-1} K^{-1}
Thermal diffusivity	κ	10^{-6}	m^2 s^{-1}
Specific heat capacity	C_P	1000	J kg^{-1} K^{-1}
Rayleigh number	Ra	$\approx 10^8$	–

2.2 Melting

In order for our models to have an evolving mantle composition, we incorporate melting which controls the chemical fractionation of bulk composition (van Heck, Davies, Elliott, & Porcelli, 2016) (a schematic for this process can be found in the supplementary material). In this implementation the solidus of dry mantle material (eq. 2) is defined as a linear function of depth (d) and composition (C, where $C = 0$ is harzburgitic material, $C = 0.25$ is ambient mantle material and $C = 1$ is entirely basaltic);

$$T_{\mathrm{solidus,dry}}(d, C) = T_{\mathrm{meltsurf}} + dT_{\mathrm{meltslope}} + (1 - C)T_{\mathrm{meltcomp}}. \tag{2}$$

For this study $T_{\mathrm{meltsurf}} = 1200\,\mathrm{K}$, $T_{\mathrm{meltcomp}} = 500\,\mathrm{K}$ and $T_{\mathrm{meltslope}} = 2.5\,\mathrm{K\,km}^{-1}$.

Since we are now able to accurately track the movement of water within our 3-D model we extend our previous dry solidus definition to account for the influence of water on melting. We do this by extending eq. 2 using the parameterisation of Katz et al. (2003) such that the solidus of wet material is found via;

$$T_{\mathrm{solidus,wet}}(d, C, C_w) = T_{\mathrm{solidus,dry}} - 43C_w^{0.75}. \tag{3}$$

117 Dry and wet solidus temperature profiles for our model are shown in the supplementary
118 material.

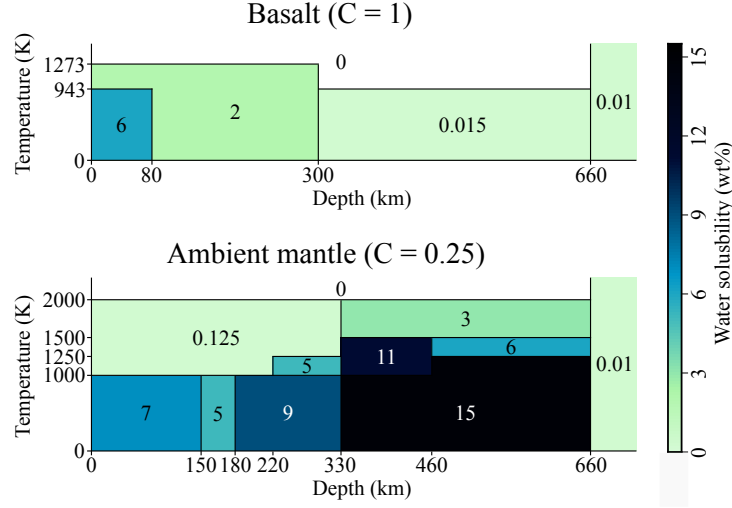### 2.3 Water Transport

Figure 1. Water solubility used in this study.

120 To accurately model the movement of water within the mantle (beyond the advec-
121 tion of the particles within the model) we consider three additional processes of water
122 transportation: dehydration, rehydration and melting. These processes link mantle wa-
123 ter content to the model's finite external ocean reservoir, thus allowing us to ensure the
124 total OM in the model is conserved between the mantle and ocean.

125 Dehydration is performed when a particle holds more water than is possible for its
126 given depth, temperature and composition, denoted as $C_{w,\max}(d, T, C)$ (Fig. 1). At each
127 time step following the movement of the particles, each particle is checked to ensure its
128 water content C_w does not exceed the particle's saturation value $C_{w,\max}$. The method
129 used to move any excess water is modelled after Nakagawa et al. (2015); whereby the ex-
130 cess water of a particle ($C_{w,\mathrm{ex}}$), is transferred vertically towards the surface until it reaches
131 a particle that is not saturated. If no further vertical movement is possible then the ex-
132 cess water is transferred to the external ocean reservoir (a schematic for this process can
133 be found in the supplementary material). Saturation values for basalt and the ambient
134 mantle are similar to those used in Nakagawa et al. (2015), which are based on the sol-
135 ubility phase diagrams of Iwamori (2007). In order to determine the saturation value $C_{w,\max}$

of any C material that lies between these two tables, appropriate values are obtained via linear interpolation; whereas for $C < 0.25$, values are taken from the ambient mantle table (eq. 4).

$$C_{w,\mathrm{max}}(d, T, C) = \begin{cases} C_{w,\mathrm{amb}}(d, T) & \text{for } 0 \leq C < 0.25 \\ C_{w,\mathrm{amb}}(d, T)(1 - \alpha_C) + C_{w,\mathrm{bas}}(d, T)\alpha_C & \text{for } 0.25 \leq C \leq 1, \end{cases} \tag{4}$$

where $C_{w,\mathrm{amb}}$ and $C_{w,\mathrm{bas}}$ are the water solubility values for the ambient and basaltic material as taken from the Fig. 1 and $\alpha_C = (C - 0.25)/0.75$ is used to interpolate for values of $C_{w,\mathrm{max}}$ between the two end members.

Outgassing is the second process of water movement and occurs when a particle undergoes a melting event. Upon melting, water is partitioned into the melt (with a partition coefficient $D = 0.01$). The water mass contained within the melt is then instantaneously transported to the surface and outgassed into the ocean.

Rehydration is a process at the surface boundary layer of the model domain whereby for any surface cell which has experienced melting in the current time-step, any particles it contains are saturated up to their given $C_{w,\mathrm{max}}$ value (Fig. 1) by the amount $C_{w,\mathrm{add}} = C_{w,\mathrm{max}} - C_w$ using additional water taken from the ocean. If there is not enough water available in the ocean for rehydration then the rehydration process cannot occur. Furthermore, to account for the proximity of a particle in the surface cell to the surface boundary, we multiply $C_{w,\mathrm{add}}$ by a function (here we chose the logistic function), such that a particle's water content after rehydration can be found by

$$C_w(d, T, t = t_{n+1}) = C_w(d, T, t = t_n) + C_{w,\mathrm{add}}(d, T)\left(1 - \frac{1}{1 + \exp(-s(d - d_0))}\right), \tag{5}$$

where s gives the steepness of the function's transition from 1 to 0 (here $s = 0.2 \ \mathrm{km}^{-1}$), and d_0 is half the maximum rehydration depth (here taken as the midpoint of the surface cell). Through this adaption of the rehydration process compared to previous studies (e.g. Nakagawa et al., 2015) we aim to better mimic the effects of hydrothermal circulation.

Using this logistic function we ensure that particles at the top of the cell are rehydrated to a greater degree than those at the bottom of the cell. The sensitivity of outputs to this depth dependent rehydration method is shown to be negligible, with results shown in the supplementary material. This method differs from the previous 2-D mod-

163 els of Nakagawa et al. (2018, 2015) in that we do not indiscriminately rehydrate the en-

164 tire surface to the maximum saturation value, which results in a dramatic difference in

165 the total water storage (see the supplementary material).

2.4 Parameter Space

167 In order to understand the role of different physical properties on the water stor-

168 age capacity of an Earth style mantle, we vary a range of common mantle properties.

169 Our reference case (case 005), uses parameters typically used in studies of mantle con-

170 vection and are known to produce a good first order fit to the mantle structures observed

171 on Earth (e.g. incompressible, rheologically layered, mantle convection models). The ref-

172 erence layered viscosity structure η_d is split in three layers; η_{lith} from 0-100 km depth,

173 1 for the remainder of the upper mantle and η_{660} below 660 km depth.

174 From the reference case we vary a number of the model's physical parameters (out-

175 lined in Table 2) including; the radial viscosity factors and viscosity laws, compositional

176 density influences, phase changes, lower mantle water solubility values, internal heating

177 and compressibility. For cases which involve lateral variations in viscosity, lateral con-

178 trasts caused by temperature and water content are controlled by the following;

$$\eta_T(T, d) = \exp(V_a z' - E_a T') \tag{6}$$

179 where $V_a = 1$ and $E_a = 2$ are non-dimensional constants that control the sensitivity

180 to depth and temperature while z' and T' are non-dimensionalised by the mantle depth

181 and $\Delta T = T_{CMB} - T_S$ respectively; and

$$\eta_w(C_w) = (1 + C_w)^{-r} \tag{7}$$

182 where r controls the water content dependence.

183 The total water within the mantle is initially 5 OM, with 0 OM present in the ocean

184 (in this paper we refer to this as a 'wet' case). We do not investigate the effects of vary-

185 ing the starting or total water content within the system on the evolution of the man-

186 tle in this work as it is beyond the scope of the present study. All our simulations are

187 run from their initial condition for 3.6 Byr, as our formulation is not suitable for mod-

188 elling a magma ocean stage which might have occurred early in Earth history.

Table 2. Case summary (ρ_{C_w} and ρ_C denote water and bulk composition density contributions, Γ_{410} and Γ_{660} denote the Clapeyron slope of the phase boundaries at 410 and 660 km depth).

Case	η (Pa s)	ρ_{C_w}/ρ_C	$\Gamma_{410}/\Gamma_{660}$ (Pa K^{-1})	Lower mantle $C_{w,\max}$ (wt%)	Equation of state	Rayleigh number (Ra)
005 **(Reference)**	$\eta(d) = \eta_0\eta_d$; $\eta_{\text{lith}} = 50, \eta_{660} = 30$	no/no	0/0	0.01%	Incompressible (Bousinnesq)	1.222×10^8
105	$\eta_{\text{lith}} = 1$	—	—	—	—	1.802×10^8
115	$\eta_0 = 2 \times 10^{22}$	—	—	—	—	8.178×10^6
125	$\eta_{660} = 5$	—	—	—	—	5.186×10^8
135	$\eta(d, C_w) = \eta_0\eta_d\eta_w, r = 0.3$	—	—	—	—	1.278×10^8
155	$\eta(d, C_w) = \eta_0\eta_d\eta_w, r = 0.8$	—	—	—	—	1.301×10^8
175	$\eta(d, T) = \eta_0\eta_d\eta_T$	—	—	—	—	1.590×10^8
185	$\eta(d, T, C_w) = \eta_0\eta_d\eta_T\eta_w, r = 0.3$	—	—	—	—	1.618×10^8
205	—	yes/no	—	—	—	1.125×10^8
215	—	no/yes	—	—	—	1.248×10^8
225	—	yes/yes	—	—	—	1.148×10^8
305	—	—	$1.5 \times 10^6/0$	—	—	1.216×10^8
315	—	—	$0/-1 \times 10^6$	—	—	1.167×10^8
325	—	—	$1.5 \times 10^6/-1 \times 10^6$	—	—	1.170×10^8
405	—	—	—	0.1%	—	1.222×10^8
415	—	—	—	Basalt 1%	—	1.222×10^8
455	—	—	—	DHMS Phase H	—	1.222×10^8
605	—	—	—	—	Compressible (Murnaghan)	1.242×10^8

3 Results

3.1 Reference Case

For our reference case we observe that the mantle loses over three of its initial ocean masses back to the surface reservoir within the first billion years (Fig. 2). Beyond 0.9 Byr the remaining amount of water held within the mantle shows little variation, with the total water content of the mantle ranging from 1.6–1.9 OM with a periodicity of around 1 Byr. This value lies well within the range of classic estimates of mantle water content (Hirschmann, 2006; Wu et al., 2018).

The breakdown of the various fluxes at the surface are shown in Fig. 2b. Here it can be seen that over the evolution of the model, dehydration provides a steady outflux of water after the initial period of water loss. Outgassing via melting provides more variability through time, as would be expected due to the time-dependent nature of the thermal structures within the mantle. The amount of water re-entering the mantle at the surface is roughly equal to the combined outfluxes. This can be best observed in the net flux shown in Fig. 2c where after 1 Byr we see that the net flow of water oscillates, with small amplitude, between favouring the mantle and the ocean over the remaining model time.

In Fig. 2d we show the radial average distribution of water over the course of the 3.6 Byr of model time. Here we see that the lower mantle remains near its prescribed maximum water capacity of 0.01 wt% for the duration of the calculation. Likewise in the upper mantle, the bulk of the displayed time-dependent lines sit within close proximity to each other, showing that there is only small variability (significantly less than 1 wt%) in the radial average through time. Within the upper mantle we can match the major changes in average water content with the shifts in the maximum water solubility table (Fig. 1).

From the high values at the surface we see a rapid drop off in the water content caused by the major reduction of C_w, max of basaltic material at 80 km depth. This continues down to 150 km where we find the choke point in the ambient mantle saturation table (as described in Nakagawa & Iwamori, 2017), after which, the rate at which the average water content decreases (radially) reduces as it approaches 300 km (the point where basaltic material's water carrying capacity drops off significantly). We then find
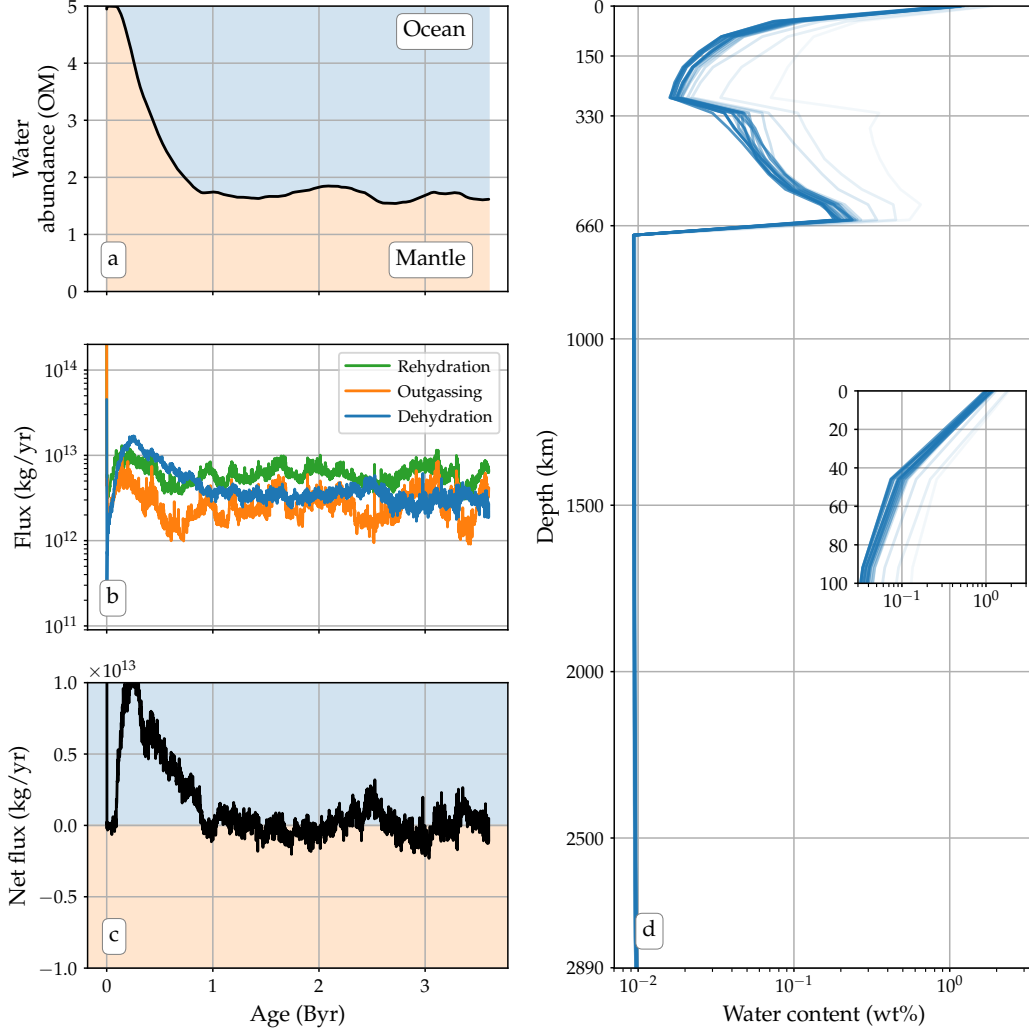
Figure 2. Outputs of mantle water storage evolution for the reference case. Shown are figures for the time evolution of; (a) water storage of the mantle, (b) the three water flux components at the surface, (c) net flux from the mantle (orange) to the ocean (blue), (d) the radially averaged water content (lines shaded according to model time; lighter - early, darker - late) with the upper 100 km highlighted on inset axis.
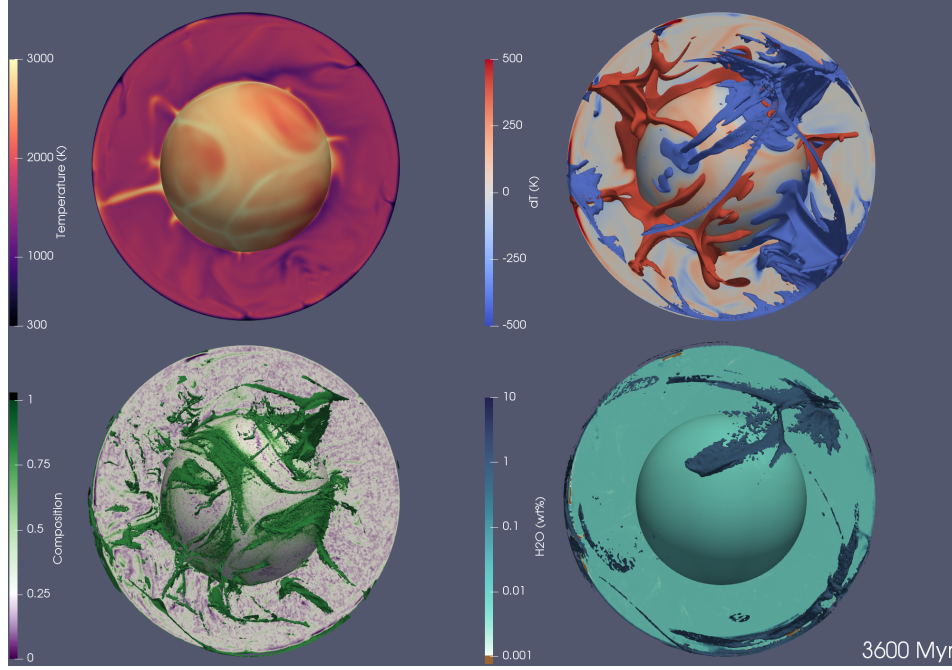
Figure 3. Output showing one hemisphere together with the CMB for the reference case after 3.6 Byr. Outputs (clockwise from top left) are; absolute temperature (K), temperature variation (K) with ±400 K isosurface, water content (wt% - noting the log scale) with 1 wt% isosurface, composition (C) with 0.8 isosurface. It can be seen that the water rich regions coincide with areas of colder than average material, with other areas of higher and low water concentrations also interspersed within the entire mantle domain.

that from 330 km down to the upper-lower mantle boundary at 660 km, the average mantle water content increases due to the large storage capacity of ambient mantle material colder than 1500 K (up to 15 wt%). The sharp decrease below 660 km is due to the dehydration of any material passing through into the lower mantle, where the maximum water content is fixed to 0.01%.

We show one hemisphere from the final output of our reference case in Fig. 3. Here it is possible to gain a better understanding of the lateral variations of the model, in particular the distribution of water. The 1 wt% isosurface shows the particularly wet regions within our reference case, with these zones aligning with the major cold regions at the surface. Particularly dry regions are also observed (brown regions) where plume features reach to the near surface. These regions in the model would be expected to contain very little water due to their high temperature and from outgassing via magmatism.
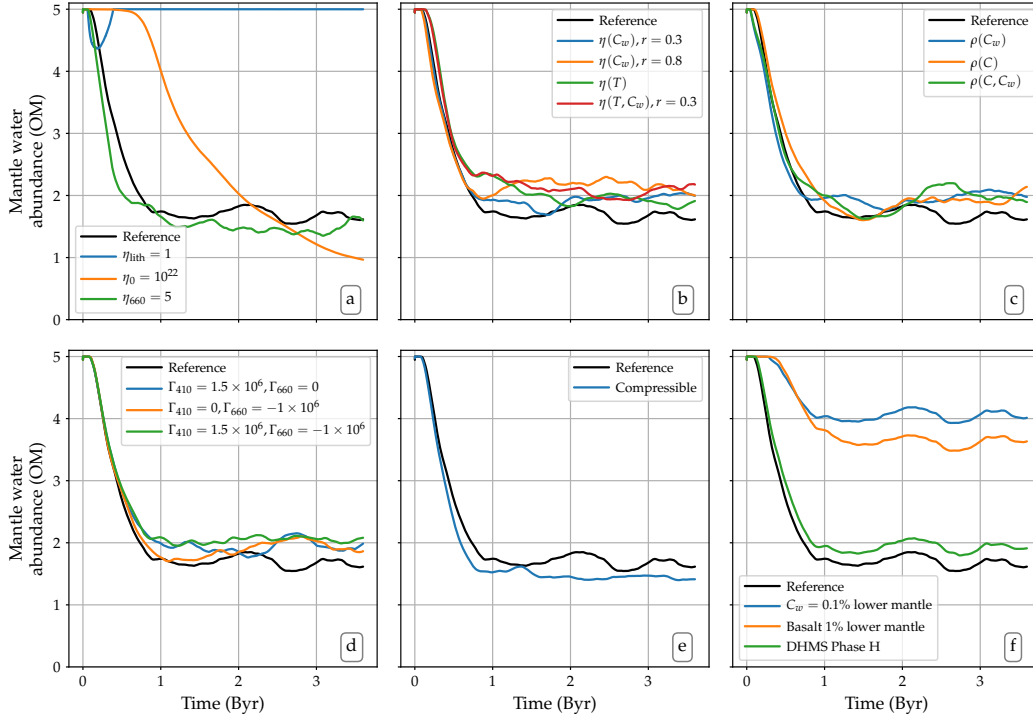
Figure 4. Mantle water storage evolution for the cases detailed in Table 2. After 3.6 Byr the majority of the cases examined have reached a mantle water abundance within 0.5 OM to the reference case.

Beyond the significantly hot and cold features at the near surface we note that the mantle water content appears fairly homogeneous, implying that the water is well mixed throughout the volume. Within this figure we can also observe the movement of basaltic material as it is transported into the lower mantle in the cold downwelling material, before being brought back up to the surface in plumes.

3.2 Viscosity Variation

3.2.1 Radial Variation

We begin considering the influence of the various parameters by investigating the effect of altering the reference case's radial viscosity structure. Altering the radial viscosity structure has a major impact on the models convective vigour, fundamentally changing how efficiently the mantle may cool. For the three cases we explore we look at the
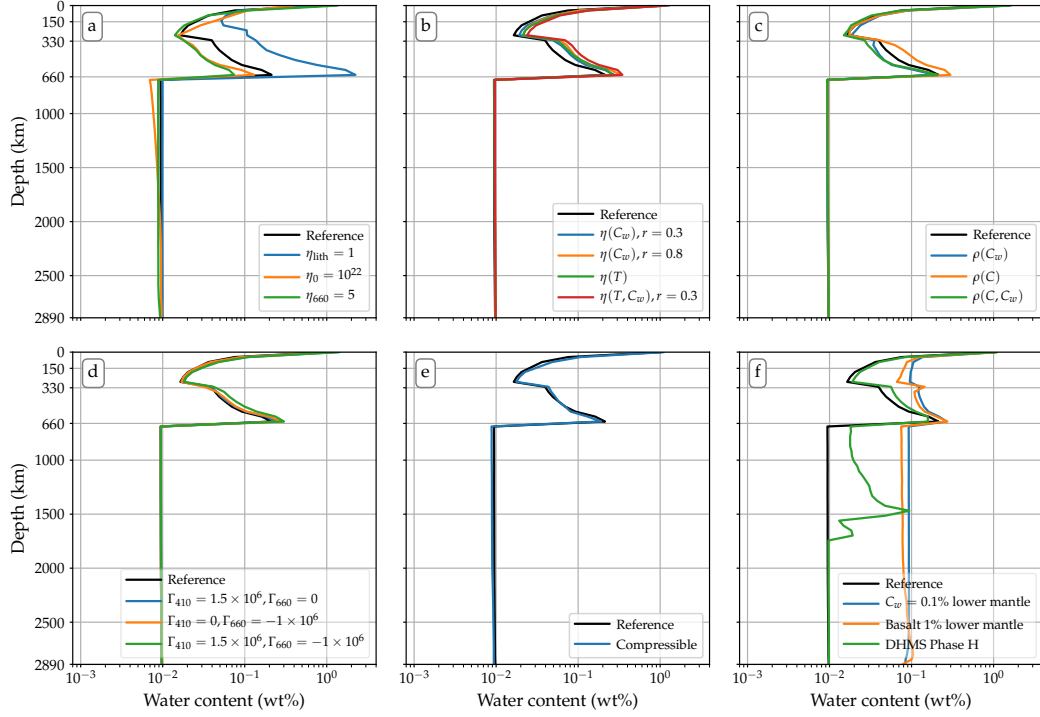
Figure 5. Radially averaged water content after 3.6 Byr for the cases detailed in Table 2 (zoomed in figure of the top 100 km can be found in the supplementary material). It can be seen that the radial average across the cases broadly reflects the changes in saturation values from the tables, with distinct jumps at the base of the lithosphere, 300 km, 330 km and 660 km depth.

effects of; removing the increase in the lithosphere viscosity, reducing the viscosity jump into the lower mantle and increasing the reference viscosity η_0 by an order of magnitude.

We find that these three cases all have significant, but different effects on the temporal water storage profiles shown in Fig. 4a. By having no high viscosity lithosphere, the mantle is able to rapidly cool and we find that within half a billion years the mantle is sufficiently cold to store all 5 OM. Any water that is lost via dehydration or outgassing is small enough that it is easily passed back into the mantle via rehydration. Reducing the lower mantle viscosity jump on the other hand does not have much effect on the water being stored compared to the reference case, as whilst the mantle will convect more readily, the heat lost at the surface is still limited by the viscous lithosphere.

In the final case, increasing the reference viscosity causes the thermal boundary layers to thicken, meaning that the average temperature is colder to a greater depth compared to the reference. Whilst this allows more water to be stored (according to the assumed saturation values) it also results in a reduction in magmatic activity, resulting in reduced outgassing and crucially much less rehydration. This can be evidenced in the much gentler, monotonically decreasing mantle water abundance for this case, which is still decreasing to below 1 OM after 3.6 Byr. Therefore the net effect of increasing the thermal boundary layer is to lower the amount of water being stored within the mantle after 3.6 Byr.

The radial distribution of the water at the end of the calculations highlights how the different radial viscosity profiles are altering where, and how much, water can be stored (Fig. 5a). The effect of significantly lower mantle temperatures caused by the cooled mantle (due to $\eta_{\text{lith}} = 1$) is clear in the average radial distribution of water, with an order of magnitude greater wt% water being stored in much of the upper mantle compared to our reference case. This is due to much more of the upper mantle being at the cold temperatures where the mantle is predicted to exist as phases with much greater water carrying capacity. The other two cases both hold less water in the main water carrying region of the mantle (up to 15 wt% between 330–660 km depth), but display differing average amounts at shallower depths. The effect on the near surface thermal boundary layer caused by increasing η_0 results in much more water stored at shallow depth, but a reduced amount of water present at the surface layer due to the previously mentioned lack of rehydration (see Fig. S4). Meanwhile, decreasing the lower mantle viscosity does not

275 alter the overall storage capacity of the mantle compared to the reference case, we con-

276 clude that the water not being stored between 330–660 km depth is instead being held

277 in the uppermost region of the mantle (Fig. S4).

3.2.2 Lateral Variation

279 We also investigate the effect of additional lateral viscosity variations on top of our

280 radial viscosity structure through the influence of both thermal and water variations. For

281 the water dependent cases, we investigate both a high and low viscosity dependence on

282 water variation. Results for the water storage and radial average are shown in Figs. 4b

283 and 5b respectively. In contrast to the previous radial cases which produced significant

284 shifts in the total mantle water, all lateral variations considered yield a moderate increase

285 in water storage within the mantle over 3.6 Byr. This is due to the higher convective vigour

286 of the lateral cases causing an increase in the surface mobility. The increase in the sur-

287 face velocity leads to lower mantle temperatures as heat is lost through the surface at

288 a greater pace compared to the other cases, allowing more water rich phases within the

289 saturation tables to be accessed (a figure of the average radial temperature profiles at

290 the end of the calculations for these cases can be found in the supplementary material).

3.3 Density Variation

292 We also investigate three cases where the density field is influenced by the chem-

293 istry of the particles; bulk composition only $\rho(C)$, water only $\rho(C_w)$ and a combination

294 of both bulk composition and water $\rho(C, C_w)$. When the bulk composition affects den-

295 sity, basaltic material is denser in the upper (by 4%) and lower mantle (3%), but is lighter

296 (-5%) between 660-740 km depth to mimic a basalt barrier (G. F. Davies, 2008). Wa-

297 ter meanwhile, makes material 0.25% lighter for every 1 wt% water.

298 From Fig. 4c we see that any density influence causes an increase in the total man-

299 tle water storage throughout the calculation by up to $\approx 30\%$ compared to the reference

300 case. Looking at the radial average water content (Fig. 5c), the $\rho(C)$ case stands out as

301 having more water between 330–660 km depth compared to the reference and other den-

302 sity cases. From our saturation tables (Fig. 1) we see that this is the region where the

303 ambient mantle can store most water while basalt can hold very little. As basalt is denser

304 in the upper mantle for this case, we find that there is less basaltic material in this re-

gion and so there is more high water carrying low C material present causing the observed water increase. Meanwhile, all other density cases display lower radial average water content than the reference case in this same region. Despite this, all these cases contain an increased average water content wt% in the uppermost layers (of 0.1 to 1 %) compared to the reference.

3.4 Phase Changes and Equation of State

The inclusion of a phase change at either or both boundaries at 410 and 660 km depth (Bunge et al., 1997; Tackley, Stevenson, Glatzmaier, & Schubert, 1994) all result in similar increases in the total mantle water abundance as the density cases (Fig. 4d). A phase change at 410 km depth enables the cold downwelling material to descend quicker into this region resulting in an increase in the presence of colder than average material which allows more water to be stored. At 660 km depth meanwhile, the negative Clapeyron slope serves to inhibit convection resulting in cold downwelling material to take longer to cross this boundary while also slowing down any hot upwelling material. The net effect of this phase transition is to also allow the upper mantle to be at a reduced temperature compared to the reference, hence the higher observed water storage.

It could be expected that using a compressible equation of state for the mantle could result in a shift in the amount of water able to be held within the mantle. To this end we employ a Murnaghan equation of state (where we also set $T_{CMB} = 4000$ K). The shift in temperature structure caused by compressibility however, has little effect on the amount of water being held within the mantle (Fig. 4e) with ≈ 1.5 OM compared to the references 1.7 OM after 3.6 Byr. This is because the adiabatic temperature profile between the two boundaries means that for most of the upper mantle, average radial temperatures are similar to the incompressible cases (the radially averaged mantle temperatures for this case can be found in Fig. S6). Meanwhile in the lower mantle, where there are higher temperatures compared to the reference, our saturation values are insensitive to temperature so we see no difference.

Looking at the radially averaged water content profile of the compressible case (Fig. 5e) we identify that the region where less water is being stored compared to the reference case is from around 500 km depth to the upper-lower mantle transition. We find that this is where the radial temperature profile of the compressible case begins to exceed the

reference case (see Fig. S6). This also has a small effect on the water held in the lower mantle, as there is slightly less water available to be carried into the lower mantle via down-going material to replace the water being carried in upwelling material.

3.5 Changes to Lower Mantle Water Saturation Assumptions

The final cases we investigate concern the assumed saturation levels of the lower mantle. For this we consider three additional variations of our reference model. The first case involves simply increasing the lower mantle water storage capacity by one order of magnitude to 0.1 wt%. Our second case assumes that basaltic material is able to hold up to 1 wt% water in the lower mantle as a simple example for studies suggesting slabs transport water through the lower mantle down to the CMB (Mao et al., 2017; Ohira et al., 2014). Finally, we more accurately consider a varying water carrying capacity for water in the lower mantle by introducing the effects of a phase H within dense hydrous magnesium silicate (DHMS) (Nishi et al., 2014; Ohtani, 2015). The implications of including phase H is to introduce a lower mantle water reservoir between 660–1700 km depth in cold ambient mantle material which can hold up to 8 wt% water (the full water solubility map comparable to Fig. 1 for this case, which includes DHMS phase H, can be found in the supplementary material).

From Fig. 4f we find that the amount of water stored in the mantle is increased for these three cases. Unsurprisingly a blanket increase in $C_{w,\max}$ in the lower mantle greatly enhances the amount of water being held after 3.6 Byr, as the lower mantle accounts for two-thirds of the mantle volume. For this case we find that the mantle is holding ≈ 4 OM at the end. Of particular note is that we see from the radial profile (Fig. 5f) that, whilst the lower mantle average is much higher than the reference, the upper mantle also stores a greater amount of water. This occurs because upwelling material from the lower mantle is now an order of magnitude wetter than the reference.

We see broadly similar results for the case where basalt carries 1 wt% water in the lower mantle, despite the majority of material in the lower mantle being ambient material. This case holds around half an ocean mass less of water compared to the previous case after 3.6 Byr, and radially stores a similar amount of water throughout the mantle. Of note is the small increase in average water content in the lowermost 500 km for

this case compared to the previous case. There is no compositional density influence in this case so we cannot attribute this increase to the influence of dense basaltic material.

The final case is in response to mineral physics studies which suggest that there may be hydrous phases that can exist at the pressures of the lower mantle (Ohtani, 2015). Dense hydrous magnesium silicate (DHMS) phase H could be capable of carrying up to 12 wt% water in the upper portions of the lower mantle, and has been considered in the 2-D numerical model study of Nakagawa et al. (2018). Similar to Nakagawa et al. (2018), we prescribe a region extending from a depth of 660 km down to 1700 km for temperatures colder than 1500 K which has a water saturation value of 8 wt%. We see that this extension of the solubility map for ambient material has a minimal effect on the overall water budget of the mantle through time, only allowing approximately 0.2 OM extra to be stored over the time period. Radially, we see that the inclusion of the DHMS phase H changes the mid mantle average water content. Now that more water can be carried through 660 km, the sharp peak seen in the reference case as water is dehydrated from down-going material is removed. Instead the main peak is now located around 1500 km, where only cold material (< 1000 K) can continue to hold a significant amount of water.

4 Discussion

4.1 Mantle water storage sensitivity

Based on our results it is apparent that varying parameters of the mantle dynamics within reasonable ranges has a limited effect on the mantle's long term water storage capacity. We do however find that, whilst most of the cases examined hold relatively similar amounts of water in the mantle (1.6–2.1 OM), different physics can alter at what depth this additional water is stored. For instance, for the different density cases considered, we find that the inclusion of water dependency shifts the water storage in the transition zone to lower average values compared to the reference case. As we have here only considered water making a minor contribution to the buoyancy field, careful consideration will have to be made when attempting to reconcile these numerical models with inferences of transition zone water distribution (e.g. Wang, Pavlis, & Li, 2019) if also considering a water dependent density field in the mantle.
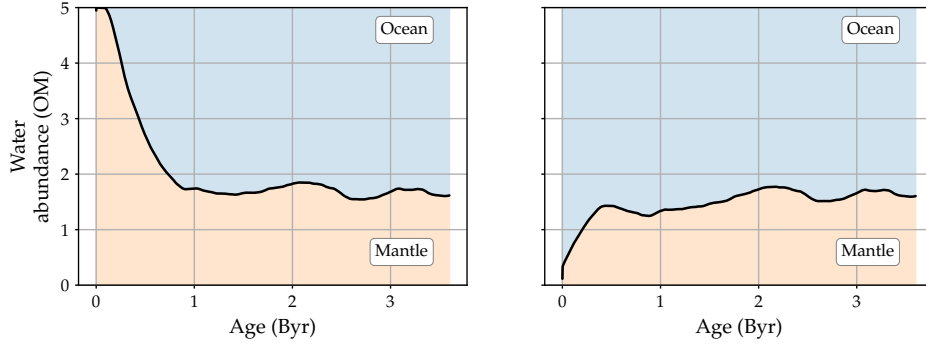
Figure 6. The mantle water storage evolution for different locations for the water in the initial condition of the reference case. (Left) the reference case which contains 5 OM in the mantle and 0 OM in the ocean reservoir at initiation, a wet mantle initial condition. (Right) the reference case model but now with 0 OM in the mantle and 5 OM in the ocean reservoir at initiation, a dry mantle initial condition. It can be seen that by 2 Byr, the distribution of water between the mantle and the ocean is very similar in the two cases and is virtually indistinguishable by 3 Byr.

For the cases where we change the mantle dynamics, it is the cases where the radial viscosity profile is varied that produce the most significant changes in mantle water content. This is because the change in viscosity fundamentally alters the heat loss from the modelled mantle leading to our two extreme end members for mantle water storage. In particular, we note that the case where $\eta_{\text{lith}} = 1$, whose mantle held all the available water throughout the majority of the calculation due to its significantly colder state. To better understand how much water this case could hold it was re-ran with an initial amount of water within the mantle of 10 OM. From this we found that this case stabilises with roughly 7 OM held in the mantle, a value more in line with the recent results published by Nakagawa et al. (2018).

In order to gain a sense of the sensitivity of our results to the initial water content of the mantle, we reran our reference case with a 'dry' mantle starting condition instead of the 'wet' mantle as in all other cases. Instead of starting with 5 OM in the mantle and 0 OM in the ocean (the wet case) we ran with 0 OM in the mantle and 5 OM in the ocean (the dry case). We present the temporal evolution of the wet and dry runs of the reference case in Fig. 6 (with a full breakdown of the fluxes and radial averages contained in the supplementary). It can be seen that after 500 Myr the dry case has taken up al-
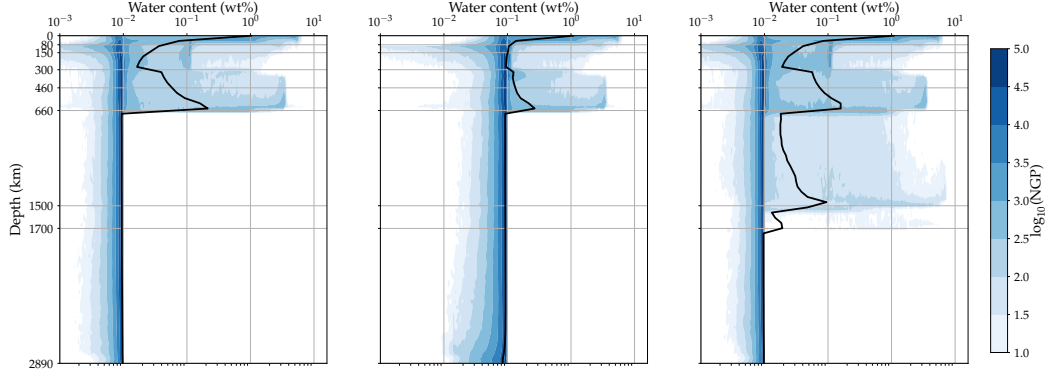
Figure 7. Histograms displaying the distribution of water content values for the different lower mantle saturation values contoured by the logarithmic colour scale according to the number of grid points (NGP) of the model mesh at each radial layer. Black lines denotes the radial averaged value. (Left) the reference case where $C_{w,\max} = 0.01$, (middle) where $C_{w,\max} = 0.1$, (right) where DHMS phase H is included in the lower mantle $C_{w,\max}$ values. It can be seen that the major concentration of points in the upper mantle is closely linked with the lower mantle $C_{w,\max}$ values.

most 1.5 OM into the mantle, and by 2 Byr contains a very similar amount of water as the wet case. By 3.6 Byr the difference in water abundance between the two cases is negligible suggesting that the mantle can efficiently distribute water from the ocean at the surface throughout the whole mantle (the supplementary videos with this paper show how the wet and dry cases converge to a very similar state). This result suggests that the present day mantle water abundance could be insensitive to its early history water content, however, there is much more investigation that needs to be undertaken looking at cases where water has feedback on the system.

4.2 Pathways to cause large changes in mantle water storage

Looking beyond the more minimal change in total mantle water storage observed in the cases where we varied the underlying physics controlling the convection in the system; the pathway that allows the largest change in mantle water storage is when the underlying saturation values were varied. We have found that changes in the poorly constrained $C_{w,\max}$ value in the lower mantle can cause this region to become a significant water storage zone.

In Fig. 7 we present a detailed look at the radial distribution of water for the cases where we altered the lower mantle $C_{w,\text{max}}$ values. The most noticeable feature in all these figures is that the vast majority of points in the upper mantle are concentrated around the lower mantle $C_{w,\text{max}}$ value. For the reference case, the bulk of the upper mantle water content is around 0.01 wt%, whereas if $C_{w,\text{max}} = 0.1$ in the lower mantle, a similar pattern is seen in the upper mantle. Upon reflection this is unsurprising, as material rising from the lower mantle will naturally emerge into the upper mantle with a water content in line with the lower mantle $C_{w,\text{max}}$ value. This trend is also observed in the case where we included DHMS phase H, with very little change in the upper mantle compared to the reference case that did not include phase H in the saturation tables.

In the transition zone, it can be seen that the distribution becomes slightly bi-modal, with a second, albeit weaker, peak around 3 wt%. This peak appears independent of what is going on at depths below 660 km for $C_{w,\text{max}}$, but is slightly more pronounced when DHMS phase H is included. There is one final significant peak from 300 km up to the surface which will be due to subducting, basaltic material, although this signal is masked by the main peak in the $C_{w,\text{max}} = 0.1$ case. The additional water storage available in the lower mantle due to phase H produces a small peak at the 1500 and 1700 km boundaries but can be seen to not shift the main concentration from 0.01 wt%.

From this we can conclude that better constraints on the lower mantle $C_{w,\text{max}}$ values will not only constrain the water storage of the lower mantle, but can be expected to cause a similar change in the upper mantle. Additionally, the clear presence of lateral variations in the water content highlight the need for these investigations to be carried out using three-dimensional models.

4.3 Comparison to previous studies

When comparing the results of this study to the most similar study (Nakagawa et al., 2018), we note a major discrepancy between the values, with our typical mantle water holding capacity going from the initial 5 OM down to ≈2 OM after 3.6 Byr (without any inclination to hold more than the 5 OM available, apart from the previously discussed case), whilst in Nakagawa et al. (2018) the mantle holds nearer 10 OM. This is clearly a conflicting pair of results, and based on our findings we attribute this to a combination of our choice in rehydration scheme (see supplementary material) and the over-
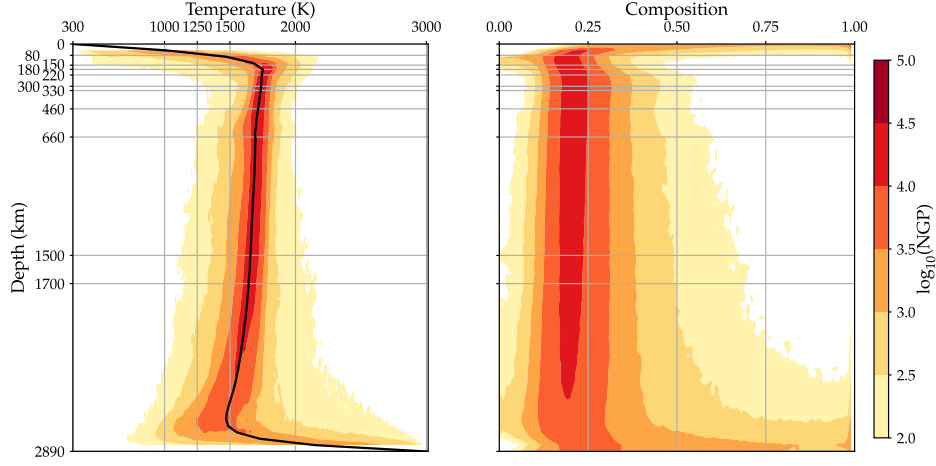
Figure 8. Histograms displaying the distribution of temperature (left) and composition (right) values for the reference case, contoured by the logarithmic colour scale according to the number of grid points (NGP) of the model mesh at each radial layer. The overlain axis grid align with the boundaries found in the saturation tables used within this study. Black line denotes the radial averaged temperature value.

all thermal structure of the mantle. In Fig. 8 we see that for our reference case the majority of points in our model sit above 1500 K, which according to the saturation tables, results in a limited amount of water being able to be stored. It is only points which sit below 1250 K which we can expect to hold substantial amounts of water (up to 15 wt%), points which we find are uncommon in the upper mantle. Of course, the reference case is not considering DHMS effects in the lower mantle as in Nakagawa et al. (2018), but we found that this also has only a minor contribution to additional water storage. We recognise though that we have not run a case with DHMS and a water dependent viscosity for example, which could increase the convective vigour of the system. However, we note that the case with a reduced lower mantle radial viscosity factor still holds a volume of water comparable to the reference case. This result combined with the conclusions that water would have only a negligible role on lower mantle viscosity (Muir & Brodholt, 2018), leads us to conclude we should not expect any lower mantle saturation changes combined with a water-dependent rheology to alter the mantle water storage beyond what the saturation values allow.

In fact the only case in this study which yields a value near to 10 OM is our reduced lithosphere viscosity case, which has a surface RMS an order of magnitude higher

476 than any other case, peaking early on at nearly 30 cm yr^{-1}; a figure which falls in line

477 with the RMS values found in Nakagawa and Spiegelman (2017) for their strongly water-

478 dependent viscosity cases. Such high surface RMS values translate to a high turnover

479 of mantle material, allowing the rapid cooling of the mantle and giving rise to high wa-

480 ter storage potential. Models in both our study, and the models in Nakagawa and Spiegel-

481 man (2017) which have surface RMS values in line with recent plate tectonics (of order

482 1 cm yr^{-1}), simply cannot cool at such rapid rates, limiting the volume of water in the

483 mantle to 1–2 OM.

484 Comparing our results to the simpler one-dimensional models we note that within

485 our models we see many instances of local lateral and temporal variations in tempera-

486 ture, bulk composition and the water content that cannot be represented in those mod-

487 els (as seen in Fig. 3 and supplementary movies, or the bimodal distributions of water

488 content in Fig. 7). These findings, together with the time-dependence therefore cannot

489 be approximated by a simple thermo-chemical evolution model. Though we have not un-

490 dertaken simple thermo-chemical evolution models here (as it would require a further

491 large study), it is clear from our results that while some of the average behaviour maybe

492 could be captured in such a model, the lateral and temporal variability show that it would

493 be very unclear what average values to give reservoirs and processes a-priori. While we

494 might imagine that such simple models could allow this work to be extended, we believe

495 they could not have been produced a-priori.

4.4 Limitations

497 One of the limitations in this study is the numerical cost of running long evolution,

498 high-vigour convection models at high resolution. As resources are not infinite, the res-

499 olution of the models we have presented are one level lower than typical current 3-D mod-

500 els (e.g. D. R. Davies et al., 2012; J. H. Davies, 2005), giving the average grid spacing

501 of ≈ 44 km. Because of this grid spacing, some finer features which could be generated

502 by flows in very low viscosity regions would not be resolved in our models presented. To

503 ensure sufficient resolution and numerical stability we have restricted the local viscos-

504 ity (which can vary laterally with temperature and water content) to the interval $\eta \in$

505 $[9 \times 10^{20}, 2 \times 10^{23}]$ Pa s. This limitation on the lateral variations was only reached in

506 the upper mantle. Also at higher resolution there is a denser coverage of particles within

507 the model. To this end we reran our reference case at higher resolution (with an aver-

age grid spacing of 22 km), and found that this results in only a minor effect on the total mantle storage (see the supplementary material Fig. S12).

In the models presented, we do not distinguish between the near surface water fluxing (i.e. water that leaves, then immediately re-enters the mantle each time step) and the water that is reintroduced at the surface, retained and transported deeper into the mantle. We anticipate future modelling would benefit from measuring these two different cycles, as these models could further be tested against other methods which predict the water flux over these domains (e.g. Parai & Mukhopadhyay, 2012).

5 Conclusions

For the first time, the movement of water within the mantle is modelled in three-dimensions by adapting the numerical code TERRA. The model we have developed accounts for the presence of the surface ocean and the water fluxes within the mantle in a conservative manner, whilst accounting for the three main processes of water movement; as well as the effect of water on the density and viscosity. We have modelled the movement of water within the mantle over 3.6 Byr for a variety of different physical and dynamical assumptions to investigate how the mantle's water budget evolves. In our models local lateral variations in the mantle water content are observed, highlighting the need for such studies to be conducted using these three-dimensional models.

The results of the work undertaken in this paper may be summarised as follows.

1. For the simplest mantle assumptions which are typically used in mantle modelling studies (incompressible, radially varying viscosity), the anticipated amount of water that the mantle holds is between 1.6–1.9 OM, which falls within the range expected from: petrological observations, some of the other simpler modelling studies, and recent estimates from recent planetary formation study (Wu et al., 2018).

2. The water storage capacity of the mantle only varies by a few tenths of an OM for many of the dynamic variations. Exceptions are for a particularly stiff mantle (thicker thermal boundary layers reduce ocean influx opportunity) and a very weak lithosphere (low upper boundary layer viscosity results in major heat loss from mantle) giving rise to drier and wetter mantles respectively.

3. Our models suggest the mantle can efficiently go from a dry mantle to a wet mantle over the course of 3.6 Byr, suggesting that the present mantle water content could be insensitive to its starting water content.

4. Adjusting the values used for water solubility in the mid mantle ambient material to account for a DHMS phase H does not cause a significant change in the total mantle water budget in our 3-D model.

5. We observe a close link between the lower mantle's maximum water saturation value and the upper mantle's most common water content.

As our results are noticeably different to the most comparable 2-D models, it would be pertinent to continue to study the effects of the deep-water cycle in three-dimensions. Future work will need to consider the impact of the initial mantle water budget on the role of water dependent controls such as viscosity and density; as well as to constrain such models with simple, well known observations such as one ocean mass in the surface ocean. The continued constraints on lower mantle saturation values will also prove invaluable in improving the predictions of such models. Furthermore, the addition of the assimilation of plate reconstructions and other data sources as constraints on the model evolution (e.g. Price & Davies, 2018), will undoubtably be of great benefit to the wider community as these models can begin to reconcile the spatial observations of water in Earth's mantle.

Graphs were produced using the Matplotlib package (Hunter, 2007). Images and movies were produced using Paraview (Ayachit, 2015).

References

Ayachit, U. (2015). The ParaView guide: A parallel visualization application.

Baumgardner, J. R. (1985). Three-dimensional treatment of convective flow in the Earth's mantle. *Journal of Statistical Physics*, *39*(5-6), 501–511. doi: 10.1007/bf01008348

Bunge, H.-P., & Baumgardner, J. R. (1995). Mantle convection modeling on parallel virtual machines. *Computers in Physics*, *9*(2), 207–215. doi: 10.1063/1.168525

Bunge, H.-P., Richards, M. A., & Baumgardner, J. R. (1997). A sensitivity study of three-dimensional spherical mantle convection at 10^8 rayleigh number: Effects of depth-dependent viscosity, heating mode, and an endothermic phase change. *Journal of Geophysical Research: Solid Earth*, *102*(B6), 11991–12007. doi: 10.1029/96JB03806

Crowley, J. W., Gérault, M., & O'Connell, R. J. (2011). On the relative influence of heat and water transport on planetary dynamics. *Earth and Planetary Science Letters*, *310*(3-4), 380–388. doi: 10.1016/j.epsl.2011.08.035

Davies, D. R., Davies, J. H., Bollada, P. C., Hassan, O., Morgan, K., & Nithiarasu, P. (2013). A hierarchical mesh refinement technique for global 3-d spherical mantle convection modelling. *Geoscientific Model Development*, *6*(4), 1095–1107. doi: 10.5194/gmd-6-1095-2013

Davies, D. R., Goes, S., Davies, J., Schuberth, B., Bunge, H.-P., & Ritsema, J. (2012). Reconciling dynamic and seismic models of Earth's lower mantle: The dominant role of thermal heterogeneity. *Earth and Planetary Science Letters*, *353-354*, 253–269. doi: 10.1016/j.epsl.2012.08.016

Davies, G. F. (2008). Episodic layering of the early mantle by the 'basalt barrier' mechanism. *Earth and Planetary Science Letters*, *275*(3-4), 382–392. doi: 10.1016/j.epsl.2008.08.036

Davies, J. H. (2005). Steady plumes produced by downwellings in earth-like vigor spherical whole mantle convection models. *Geochemistry, Geophysics, Geosystems*, *6*(12), Q12001. doi: 10.1029/2005gc001042

600 Davies, J. H., & Bickle, M. J. (1991). A physical model for the volume and com-
601   position of melt produced by hydrous fluxing above subduction zones. *Philo-*
602   *sophical Transactions of the Royal Society A: Mathematical, Physical and*
603   *Engineering Sciences*, *335*(1638), 355–364. doi: 10.1098/rsta.1991.0051

604 Hirschmann, M. M. (2006). Water, melting, and the deep Earth H2O cycle. *Annual*
605   *Review of Earth and Planetary Sciences*, *34*, 629–653. doi: 10.1146/annurev
606   .earth.34.031405.125211

607 Hunter, J. D. (2007). Matplotlib: A 2d graphics environment. *Computing In Science*
608   *& Engineering*, *9*(3), 90–95. doi: 10.1109/MCSE.2007.55

609 Iwamori, H. (2007). Transportation of H2O beneath the japan arcs and its implica-
610   tions for global water circulation. *Chemical Geology*, *239*(3-4), 182–198. doi:
611   10.1016/j.chemgeo.2006.08.011

612 Katz, R. F., Spiegelman, M., & Langmuir, C. H. (2003). A new parameterization
613   of hydrous mantle melting. *Geochemistry, Geophysics, Geosystems*, *4*(9), 1073.
614   doi: 10.1029/2002gc000433

615 Korenaga, J., & Karato, S.-I. (2008). A new analysis of experimental data
616   on olivine rheology. *Journal of Geophysical Research*, *113*(B2). doi:
617   10.1029/2007jb005100

618 Mao, H.-K., Hu, Q., Yang, L., Liu, J., Kim, D. Y., Meng, Y., . . . Mao, W. L. (2017).
619   When water meets iron at Earth's core–mantle boundary. *National Science Re-*
620   *view*, *4*(6), 870–878. doi: 10.1093/nsr/nwx109

621 Maruyama, S., Ikoma, M., Genda, H., Hirose, K., Yokoyama, T., & Santosh,
622   M. (2013). The naked planet Earth: Most essential pre-requisite for the
623   origin and evolution of life. *Geoscience Frontiers*, *4*(2), 141–165. doi:
624   10.1016/j.gsf.2012.11.001

625 McGovern, P. J., & Schubert, G. (1989). Thermal evolution of the Earth: effects of
626   volatile exchange between atmosphere and interior. *Earth and Planetary Sci-*
627   *ence Letters*, *96*(1-2), 27–37. doi: 10.1016/0012-821x(89)90121-0

628 McKay, C. P. (2014). Requirements and limits for life in the context of exoplanets.
629   *Proceedings of the National Academy of Sciences*, *111*(35), 12628–12633. doi:
630   10.1073/pnas.1304212111

631 Mckenzie, D. P., Roberts, J. M., & Weiss, N. O. (1974). Convection in the Earth's
632   mantle: Towards a numerical simulation. *Journal of Fluid Mechanics*, *62*(03),

633 465-538. doi: 10.1017/s0022112074000784

634 Mei, S., & Kohlstedt, D. L. (2000). Influence of water on plastic deformation of
635 olivine aggregates: 1. diffusion creep regime. *Journal of Geophysical Research:*
636 *Solid Earth*, *105*(B9), 21457–21469. doi: 10.1029/2000jb900179

637 Muir, J. M., & Brodholt, J. P. (2018). Water distribution in the lower mantle: Im-
638 plications for hydrolytic weakening. *Earth and Planetary Science Letters*, *484*,
639 363–369. doi: 10.1016/j.epsl.2017.11.051

640 Nakagawa, T., & Iwamori, H. (2017). Long-term stability of plate-like behav-
641 ior caused by hydrous mantle convection and water absorption in the deep
642 mantle. *Journal of Geophysical Research: Solid Earth*, 2017JB014052. doi:
643 10.1002/2017JB014052

644 Nakagawa, T., Iwamori, H., Yanagi, R., & Nakao, A. (2018). On the evolution of the
645 water ocean in the plate-mantle system. *Progress in Earth and Planetary Sci-*
646 *ence*, *5*(1). doi: 10.1186/s40645-018-0209-2

647 Nakagawa, T., Nakakuki, T., & Iwamori, H. (2015). Water circulation and global
648 mantle dynamics: Insight from numerical modeling. *Geochemistry, Geophysics,*
649 *Geosystems*, *16*(5), 1449–1464. doi: 10.1002/2014GC005701

650 Nakagawa, T., & Spiegelman, M. W. (2017). Global-scale water circulation
651 in the Earth's mantle: Implications for the mantle water budget in the
652 early Earth. *Earth and Planetary Science Letters*, *464*, 189–199. doi:
653 10.1016/j.epsl.2017.02.010

654 Nishi, M., Irifune, T., Tsuchiya, J., Tange, Y., Nishihara, Y., Fujino, K., & Higo,
655 Y. (2014). Stability of hydrous silicate at high pressures and water trans-
656 port to the deep lower mantle. *Nature Geoscience*, *7*(3), 224–227. doi:
657 10.1038/ngeo2074

658 Ohira, I., Ohtani, E., Sakai, T., Miyahara, M., Hirao, N., Ohishi, Y., & Nishijima,
659 M. (2014). Stability of a hydrous δ-phase, AlOOH–MgSiO2(OH)2, and a mech-
660 anism for water transport into the base of lower mantle. *Earth and Planetary*
661 *Science Letters*, *401*, 12–17. doi: 10.1016/j.epsl.2014.05.059

662 Ohtani, E. (2015). Hydrous minerals and the storage of water in the deep mantle.
663 *Chemical Geology*, *418*, 6–15. doi: 10.1016/j.chemgeo.2015.05.005

664 Parai, R., & Mukhopadhyay, S. (2012). How large is the subducted water flux?
665 new constraints on mantle regassing rates. *Earth and Planetary Science Let-*

666   *ters*, *317-318*, 396–406. doi: 10.1016/j.epsl.2011.11.024

667   Price, M. G., & Davies, J. H.   (2018).   Profiling the robustness, efficiency and limits

668   of the forward-adjoint method for 3-d mantle convection modelling.   *Geophysi-*

669   *cal Journal International*, *212*(2), 1450–1462. doi: 10.1093/gji/ggx489

670   Sandu, C., Lenardic, A., & McGovern, P.   (2011).   The effects of deep water cycling

671   on planetary thermal evolution.   *Journal of Geophysical Research: Solid Earth*,

672   *116*(B12), B12404. (n/a–n/a pages) doi: 10.1029/2011JB008405

673   Tackley, P. J., Ammann, M. M., Brodholt, J. P., Dobson, D. P., & Valencia, D.

674   (2012).   Habitable planets: Interior dynamics and long-term evolution.   *Pro-*

675   *ceedings of the International Astronomical Union*, *8*(S293), 339–349.   doi:

676   10.1017/s1743921313013136

677   Tackley, P. J., Stevenson, D. J., Glatzmaier, G. A., & Schubert, G.   (1994).   Effects

678   of multiple phase transitions in a three-dimensional spherical model of convec-

679   tion in Earth's mantle.   *Journal of Geophysical Research*, *99*(B8), 15877.   doi:

680   10.1029/94jb00853

681   van Heck, H. J., Davies, J. H., Elliott, T., & Porcelli, D.   (2016).   Global-scale

682   modelling of melting and isotopic evolution of earth's mantle: melting mod-

683   ules for terra.   *Geoscientific Model Development*, *9*(4), 1399–1411.   doi:

684   10.5194/gmd-9-1399-2016

685   Wang, Y., Pavlis, G. L., & Li, M.   (2019).   Heterogeneous distribution of water in

686   the mantle transition zone inferred from wavefield imaging.   *Earth and Plane-*

687   *tary Science Letters*, *505*, 42–50. doi: 10.1016/j.epsl.2018.10.010

688   Wu, J., Desch, S. J., Schaefer, L., Elkins-Tanton, L. T., Pahlevan, K., & Buseck,

689   P. R.   (2018).   Origin of Earth's water: Chondritic inheritance plus nebular in-

690   gassing and storage of hydrogen in the core.   *Journal of Geophysical Research:*

691   *Planets*. doi: 10.1029/2018je005698